ELSEVIER

Journal of Nuclear Materials 281 (2000) 213–224

journal of nuclear materials

www.elsevier.nl/locate/jnucmat

Heavy-ion cascade effects on radiation-induced segregation kinetics in Cu–1%Au alloys

M.J. Giacobbe [a,b], N.Q. Lam [a,*], L.E. Rehn [a], P.M. Baldo [a], L. Funk [a], J.F. Stubbins [b]

[a] *Materials Science Division, Argonne National Laboratory, Argonne, IL 60439, USA*
[b] *Department of Nuclear Engineering, University of Illinois, Urbana, IL 61801, USA*

Received 1 February 2000; accepted 5 June 2000

Abstract

Various dual ion irradiations were conducted to investigate the effect of heavy-ion cascades on the fluxes of freely migrating defects which drive radiation-induced segregation (RIS) in Cu–1at.%Au alloys. In situ Rutherford backscattering spectroscopy (RBS) was used to measure the RIS suppression effect of heavy-ion bombardment (with 300-keV Al^+, 800-keV Cu^+, and 1.2-MeV Ag^+) on 1.5-MeV He^+-RIS of Au in the near-surface region of the alloy during concurrent He^+ and heavy-ion irradiations at 400°C. Results demonstrated that the suppression of He^+-RIS correlated well with the cascade volume produced by concurrent Al^+, Cu^+, and Ag^+ irradiation per second and was independent of the weighted average primary recoil energy. Model calculations of the kinetics of RIS during dual beam irradiation were also performed and compared with the measurements. Information regarding the energetics of freely migrating point defects and their relative production efficiencies was obtained from systematic fitting. Using the values previously reported for the energies of formation and migration for vacancies and interstitials in Cu, the binding and migration energies of Au-interstitial and Au-vacancy complexes in the alloy were found to be −0.14, 0.15, and 0.03 and 0.76 eV, respectively. The respective derived efficiencies of freely migrating defect production by energetic He^+, Al^+, Cu^+, and Ag^+ ions were 0.25, 0.12, 0.09, and 0.08.

1. Introduction

Persistent fluxes of freely migrating defects (FMDs), interstitials and vacancies, which survive mutual recombination and annihilation within collision cascades and are free to migrate over distances larger than cascade dimensions, can drive local concentration changes through radiation-induced segregation (RIS) [1–3]. The production rate of FMD depends heavily on the primary recoil energy of each collision cascade as has been shown in Cu–1at.%Au [4], Ni–12.7at.%Si [5], and Mo–Re [6] alloys. As the primary recoil energy surpasses 2 keV, the FMD production efficiency decreases rapidly to only a few percent of the modified Kinchin–Pease value [4,7]. Early studies explained the rapid decrease in FMD production efficiency by intracascade effects, i.e. annihilation of FMD during the collisional and cooling phases of the parent cascade. Computer simulations which account for these intracascade effects [8,9], however, showed that primary recoil energies as high as 10 keV resulted in FMD production exceeding 10% of the modified Kinchin–Pease value, which is thus in disagreement with experimental results. Wiedersich [10,11] has suggested that cascade remnants, i.e. interstitial and vacancy clusters generated within the cascades that can act as annihilation sites for FMD produced by other cascades (i.e. an intercascade effect), might be the source of this discrepancy.

Since energetic ion impacts produce a wide energy spectrum of primary knock-on events, it is difficult to separate intracascade and intercascade annihilation effects on FMD survival. Recent Rutherford backscattering spectroscopy (RBS) measurements by Iwase et al.

* Corresponding author. Tel.: +1-630 252 4953; fax: 1-630 252 4289.
E-mail address: nlam@anl.gov (N.Q. Lam).

0022-3115/00/$ - see front matter
PII: S0022-3115(00)00330-5

in Cu–1at.%Au [5,12] and Ni–12.7at.%Si [13] alloys showed that interactions between short-lived (<1 s) cascade remnants produced by Ne^+ [12,13], Cu^+ [5,12,13], and Ar^+ [13] and FMD produced by 1.5-MeV He^+ are responsible for reducing steady-state defect populations during dual heavy and light-ion irradiations. The annihilation of FMD results in the suppression of 1.5-MeV He^+-RIS, and this suppression effect increases with increasing heavy-ion beam flux until complete suppression of He^+-induced atom transport is obtained [5,12].

In the present study, the rate effect of the production of cascade volume – a quantity related to the maximum number of displacements created by a collision cascade – by 300-keV Al^+, 800-keV Cu^+, and 1.2-MeV Ag^+ on 1.5-MeV He^+-induced Au transport in a Cu–1at.%Au alloy at 400°C was investigated. The main goal was to determine whether the intercascade RIS suppression by heavy-ion cascade remnants depends on median primary recoil energies or cascade volume production rates. The RIS kinetics during dual irradiation was also calculated, using the Johnson–Lam model [1], for various sets of physical parameters, and compared with the experimental measurements.

2. Experimental procedure

In situ RBS experiments were performed to quantify Au depletion in the near-surface region of a Cu–1at.%Au alloy during single He^+ irradiation as well as dual He^+ and heavy-ion irradiation. 1.5-MeV He^+ ions were used to both produce FMD at a high efficiency and conduct RBS measurements, while 300-keV Al^+, 800-keV Cu^+, and 1.2-MeV Ag^+ ions were chosen to create energetic collision cascades, generating cascade remnants.

The Cu–1at.%Au coupons, $1\times6\times15.5$ mm^3 in size, used in the experiment were first annealed at 960°C in 5×10^4 Pa (0.5 atm) of Ar for 17 h, mechanically polished, and finally electropolished (in a solution consisting of 65% methanol, 28% nitric acid, and 7% butyl cellusolve at −30°C) to produce a suitable surface for RBS experiments. They were then mounted on the heating stage of a goniometer in an irradiation chamber interfaced to both a 2-MeV tandem accelerator and a 650-keV ion implanter. The geometry for all single and dual irradiation experiments, shown in Fig. 1, is identical to that used previously by Iwase et al. [5,12]. Apertures for He^+ and heavy-ion beams were 1 and 3 mm in diameter, respectively, in order to ensure that heavy-ion irradiation was uniform within the analyzed area. RBS spectra of 1.5-MeV He^+ were recorded at 20-min intervals during irradiation. All RBS experiments were performed at 400°C with an error in temperature of ±10°C, and the detector was constantly cooled with dry ice to improve energy resolution.

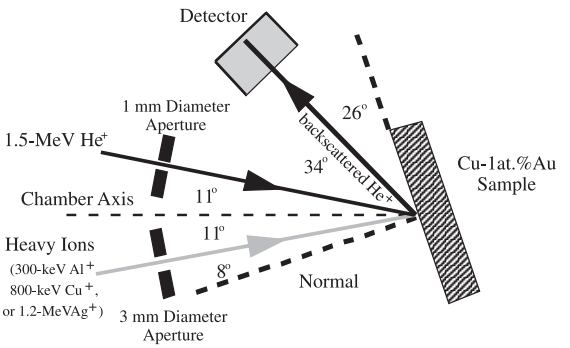

Fig. 1. Experimental geometry for 1.5-MeV He^+ RBS measurements during dual He^+ and heavy-ion (300-keV Al^+, 800-keV Cu^+, and 1.2-MeV Ag^+) irradiations in Cu–1at.%Au at 400°C. For RBS measurements during single He^+ or single heavy-ion irradiation, the same geometry is used.

2.1. Irradiation parameters

The choice of heavy ions and energies was based on weighted primary recoil spectra and the weighted average primary recoil energy, $T_{1/2}$, which is defined as the primary recoil energy below (or above) which 50% of all defects are produced. Since Iwase et al. [5,12] already reported data for dual 1.5-MeV He^+ and 800-keV Cu^+ irradiation on Cu–1at.%Au, we chose to have one type of ions with $T_{1/2}$ less than, and one greater than, that for 800-keV Cu^+. Using TRIM-96 and a displacement energy of 29 eV for Cu–1at.%Au [14], weighted primary spectra were calculated for 300-keV Al^+, 800-keV Cu^+, and 1.2-MeV Ag^+ as seen in Fig. 2. These simulations resulted in $T_{1/2}$ values of 17, 50, and 81 keV, respec-

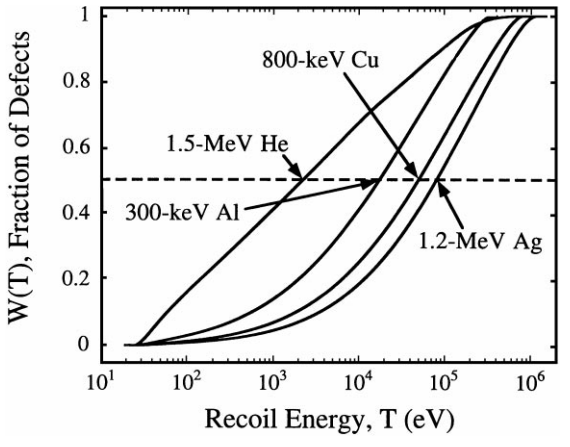

Fig. 2. Weighted primary recoil spectra for 1.5-MeV He^+, 300-keV Al^+, 800-keV Cu^+, and 1.2-MeV Ag^+ in Cu–1at.%Au as calculated by TRIM. The ordinate gives the fraction of defects produced by primary recoil collisions with energy less than T. $T_{1/2}$ values are indicated by the arrows.

Table 1
Values for damage cross sections, σ_d, $T_{1/2}$, and ranges in Cu–1at.%Au

Ion/energy	σ_d (barn)	$T_{1/2}$ (keV)	Range (nm)
1.5-MeV He^+	1.46×10^6	2.2	2380
300-keV Al^+	1.12×10^9	17	213
800-keV Cu^+	3.01×10^9	50	225
1.2-MeV Ag^+	5.80×10^9	81	200

tively. Damage cross-sections, σ_d, were also calculated using TRIM-96, over depths <100 nm, significantly larger than the thicknesses of Au depletion zones in all experiments (<60 nm). The values of $T_{1/2}$, σ_d, and ranges for all ions are given in Table 1.

Beam currents (i.e. damage rates) for 300-keV Al^+ and 1.2-MeV Ag^+ were chosen to create the same total cascade volume per second in the first 100 nm of Cu–1at.%Au as the 1- and 5-nA 800-keV Cu^+ beams implemented by Iwase et al. [5,12]. The total cascade volume was defined as the sum of peak displacement densities created by all cascades during irradiation, assuming that all displacements were closely packed in a sphere. The first step in calculating the total cascade volume was to determine the primary recoil energy, T, of each cascade event for 1000 incident ions. Then, the peak number of displacements, N, for each cascade was determined by using the relationship $N = 500\mathrm{T}(\mathrm{keV}) - 250$, which was extracted from molecular dynamics results [15]. Subcascade formation was not considered. From the values of N, the total cascade volume per incident ion, averaged over the 1000 incident ions, was obtained.

Fig. 3 gives a schematic example of the cascade distribution produced by one 300-keV Al^+, one 800-keV Cu^+, and one 1.2-MeV Ag^+ in Cu–1at.%Au. The spheres represent individual cascade events, and their sizes scale to energy by Eq. (1). The values for total cascade volume per incident ion are given in Table 2 for the three heavy ions used in this investigation. It can be seen from Tables 1 and 2 that the total cascade volume per ion increases with increasing $T_{1/2}$, and varies by about a factor of 10 from 300-keV Al^+ to 1.2-MeV Ag^+.

Using the value for total cascade volume per ion and the ion flux, the total cascade volume per second was calculated (Table 2). For the ion beam energies employed, 4-nA Al^+ and 0.5-nA Ag^+ produce approximately the same cascade volume per second as 1-nA Cu^+, while 20-nA Al^+ and 2-nA Ag^+ are approximately the same as 5-nA Cu^+. 10-nA Ag^+ was also implemented to investigate the effect of a third cascade volume production rate on RIS kinetics. The ion fluxes and corresponding damage rates, K, used in the experiment are also given in Table 2.

2.2. RBS analyses

During irradiation, Au becomes depleted near the surface of Cu–1at.%Au. Hashimoto et al. [4] demonstrated that the Au concentration change is not caused by preferential sputtering, but rather by the enrichment of Cu at the surface as a result of preferential transport of Cu atoms by the interstitial flux.

RBS spectra of He^+ were used to determine Au depletion as a function of total ion damage during single 1.5-MeV He^+, single heavy-ion, and dual He^+/heavy-ion irradiations in the alloy at 400°C. More specifically, the difference in counts in the Au-only region of the RBS spectrum (near the surface) was used to calculate Au

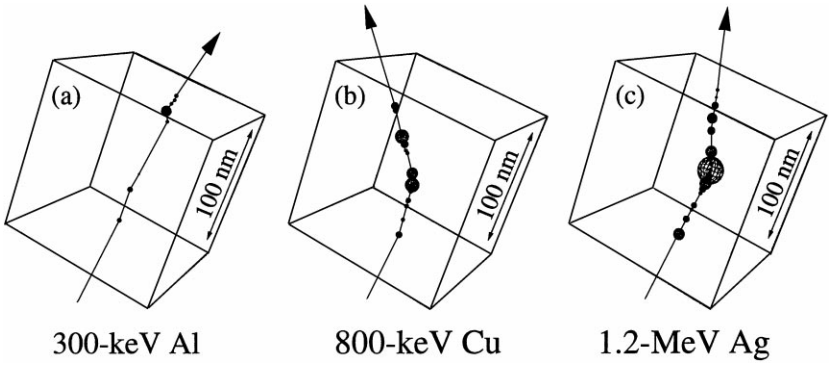

Fig. 3. Cascade damage profiles for: (a) one 300-keV Al^+; (b) one 800-keV Cu^+; (c) one 1.2-MeV Ag^+ incident on the first 100 nm of Cu-1at.%Au. The bottom surface of the cube corresponds to the sample surface while the top surface denotes a depth of 100 nm. The volume of each sphere represents the cascade volume induced by each primary cascade collision which, in turn, can be summed over many ions to determine the total cascade volume per ion. The lines through each cube represent the track of each ion through the sample.

Table 2
Values of currents, total cascade volumes per ion and per second, ion fluxes, and damage rates in Cu–1at.%Au

Ion/energy	Current (nA)	Total cascade volume per ion (10^2 nm^3/ion)	Total cascade volume per s (10^{13} nm^3/s)	Φ (ion/m^2 s)	K (10^{-3} dpa/s)
1.5-MeV He^+	100	–	–	7.96×10^{17}	0.12
300-keV Al^+	4	2.68	0.67	3.54×10^{15}	0.40
	20		3.34	1.77×10^{16}	1.98
800-keV Cu^+	1	9.63	0.60	8.84×10^{14}	0.27
	5		3.01	4.42×10^{15}	1.33
1.2-MeV Ag^+	0.5	20.6	0.65	4.42×10^{14}	0.26
	2		2.58	1.77×10^{15}	1.03
	10		12.9	8.84×10^{15}	5.13

depletion as a function of total dpa. This is clearly demonstrated in Fig. 4(a), which shows RBS spectra before and after 1.1 dpa of 1.5-MeV He^+ irradiation.

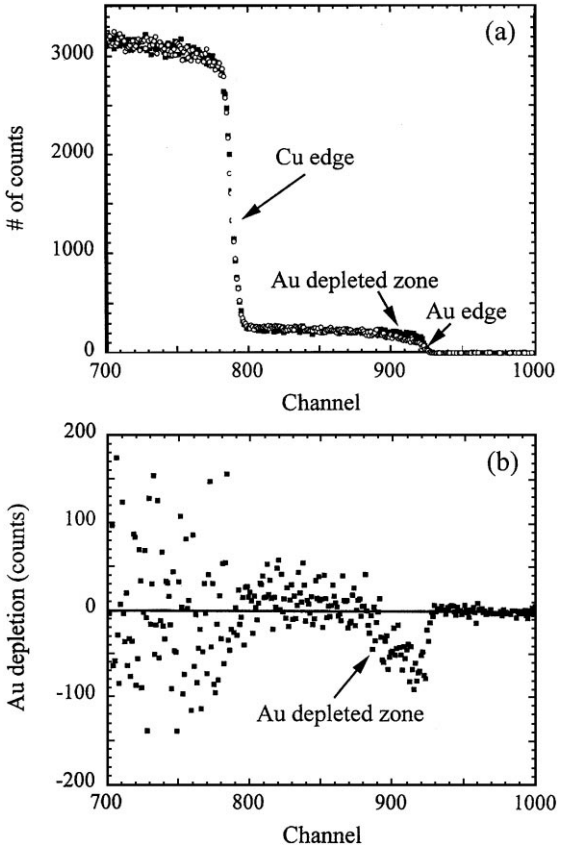

Fig. 4. (a) RBS spectra before (■) and after (○) 1.11 dpa of 1.5-MeV He^+ irradiation in Cu–1at.%Au at 400°C; (b) difference spectrum of the two spectra in (a). The difference spectrum is calculated by subtracting the 1.11 dpa spectrum from the initial pre-irradiation spectrum. The absolute value of the negative area denoted as the Au depleted zone in (b) can subsequently be measured to determine the total Au depletion in counts at 1.11 dpa.

Since the surface backscattering energies of He^+ off Cu and Au atoms at the surface are disparate, channels 800–930 contain counts from He^+, which backscattered off Au atoms only. Therefore, RBS spectra of Cu–1at.%Au have a large region in which the near-surface Au concentration changes produced by RIS can be accurately measured.

Before RBS spectra were compared to one another, they were normalized to account for varying data acquisition conditions. All spectra were normalized to a fifty-channel region, channels 701–750, where any composition changes driven by RIS were not greater than statistical fluctuations of the spectra. This region lies behind the Cu edge seen in Fig. 4(a). Small changes in incident He^+ energy result in small changes in backscattered He^+ energy, and in turn, the entire RBS spectrum shifts to lower or higher channels for negative or positive energy shifts, respectively. To account for these shifts, Au depletion calculated by difference spectra was determined through requiring conservation of Au atoms, as shown in Fig. 5. Here, the post-irradiation spectrum was shifted several times, and at each shift the difference in total counts from channel 700 to 1000, Δ_{dif}, was calculated as well as the Au depletion (determined from the difference spectrum). A linear relationship between Δ_{dif} and Au depletion was observed when Δ_{dif} was negative, and therefore, the slope, m, and y-intercept, b, were determined using a least-squares analysis. In turn, the actual Au depletion was defined by the absolute value of b and was calculated when $\Delta_{dif} = 0$, i.e. when the before- and after-irradiation spectra had the same number of counts in channels 700–1000 (conservation of Au atoms was obtained). This procedure was followed for each RBS spectrum acquired during an ion irradiation.

The error in the determination of Au depletion was defined by the error in estimating the count difference in the 'segregation-affected region' of the before- and after-irradiation RBS spectra. Indeed, if N_{unir} and N_{ir} are the respective numbers of counts, then the error in estimated Au depletion, i.e. in the difference of counts, $(N_{unir} - N_{ir})$, is simply $(N_{unir} + N_{ir})^{1/2}$.

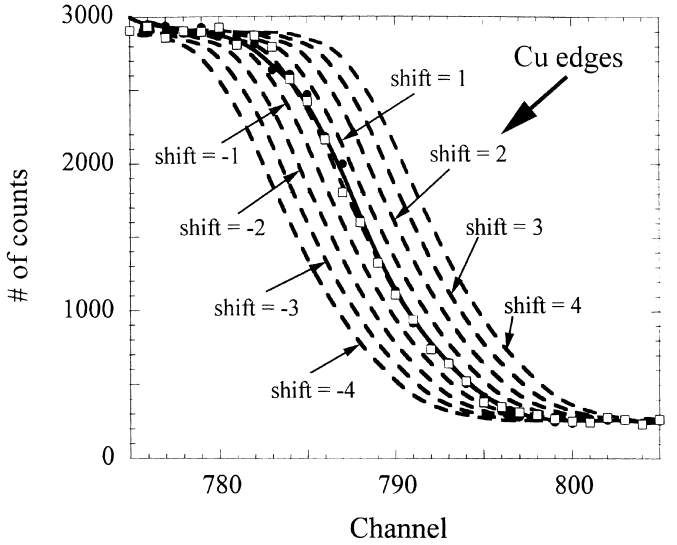

shift	Δ_{dif} (counts)	Au depletion (counts)
-4	-14521	2897
-3	-11412	2670
-2	-8209	2450
-1	-4995	2245
0	-1759	2025
1	1381	1805
2	4654	1599
3	7809	1386
4	11029	1162

using shifts -4 through 0, least squares fit analysis of Δ_{dif} (x) and Au depletion (y) gives m = -0.0679 and b = 1902 for y = mx + b

therefore, Au depletion = 1902

Note: Δ_{dif} is the difference in counts of before and after irradiation spectra in channels 700-1000

Fig. 5. Determination of Au depletion from RBS spectra before (●) and after (□) 1.11 dpa of 1.5-MeV He^+ irradiation in Cu–1at.%Au at 400°C using the conservation of mass principle. The procedure requires the after irradiation spectra to be shifted (four channels to the left and four to the right) in order to account for He^+ beam energy fluctuations during ion irradiation. To clearly illustrate the channel shifts, only the Cu edges of the RBS spectra are shown above. At each channel shift, the difference in the total number of counts from channel 700 to 1000 of the before and after irradiation spectra, Δ_{dif}, is calculated along with the absolute value of Au depletion in counts (using difference spectra similar to that in Figs. 3 and 4). Then, from a least-squares fit of the relationship $y = mx + b$ to the negative Δ_{dif} values (x) and the corresponding absolute values of Au depletion (y), the actual Au depletion (b) can be determined. For example, using shifts −4 through 0, least-square fit analysis yields $b = 1902$ counts.

3. Experimental results

The measured Au depletion in Cu–1at.%Au is plotted in Figs. 6–8 as a function of total ion damage for single 1.5-MeV He^+, single heavy-ion (300-keV Al^+, 800-keV Cu^+ [5,12], and 1.2-MeV Ag^+), and dual He^+ and heavy-ion irradiations at 400°C. (Note that RBS spectra from Iwase et al. [12 13] for Cu^+ irradiations were subject to the same analysis procedure as all other RBS data in this investigation.) Fig. 6 compares single heavy-ion irradiations with 20-nA Al^+, 5-nA Cu^+ [5,12], and 2-nA Ag^+ beams (total cascade volume production rate $\approx 3 \times 10^{13}$ nm^3/s) with corresponding dual He^+ and heavy-ion irradiations using the same Al^+, Cu^+, and Ag^+ beam currents. Fig. 7 compares 4-nA Al^+, 1-nA Cu^+ [5,12], and 2-nA Ag^+(total cascade volume production rate $\approx 6.5 \times 10^{13}$ nm^3/s) single and dual beam experiments. Fig. 8 shows the effects of three different cascade volume production rates generated by 0.5-, 2-, and 10-nA Ag^+ during single Ag^+ and dual He^+ and Ag^+ irradiations. In all cases, the total dpa was calculated using the σ_d and Φ values listed in Tables 1 and 2. Each ion irradiation data set in Figs. 6–8 was, in turn, used to establish a linear relationship (weighted least-squares analysis) in order to determine the Au depletion as a function of total dpa for each irradiation. The depletion rates, M_{dep} (counts/total dpa), along with errors,

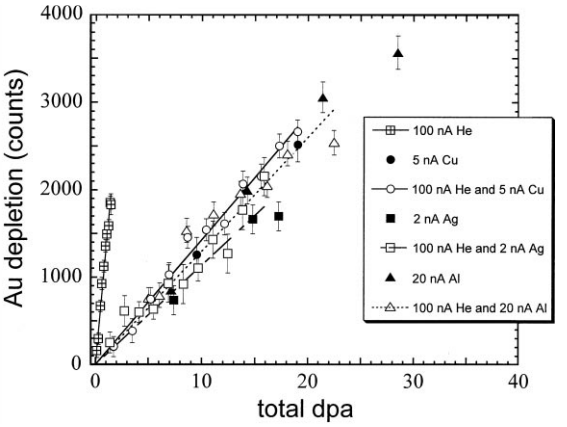

Fig. 6. Au depletion as a function of total dpa for single 1.5-MeV He^+ (⊞), single 800-keV Cu^+ (●), single 1.2-MeV Ag^+ (■), single 300-keV Al^+ (▲), dual 1.5-MeV He^+ and 800-keV Cu^+ (○), dual 1.5-MeV He^+ and 1.2-MeV Ag^+ (□), and dual 1.5-MeV He^+ and 300-keV Al^+ (△) irradiations using heavy-ion beam currents which resulted in a total cascade volume production rate of approximately 3×10^{13} nm^3/s. For dual beam irradiation experiments, the total dpa represents the sum of dpa from both ion beams. Ion beam currents are given in the legend, while depletion rates, M_{dep}, for the above experiments are listed in Table 2.

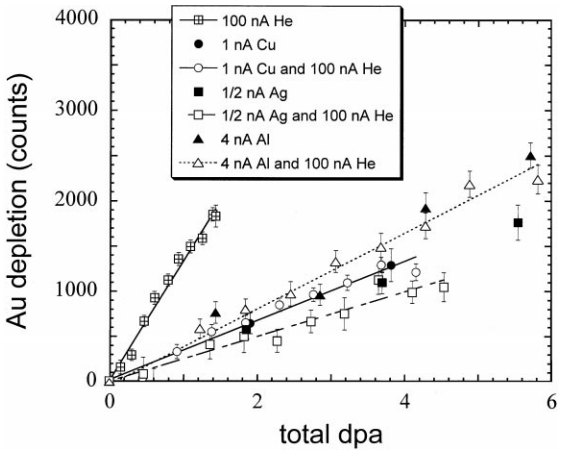

Fig. 7. Au depletion as a function of total dpa for single 1.5-MeV He^+ (⊞), single 800-keV Cu^+ (●), single 1.2-MeV Ag^+ (■), single 300-keV Al^+ (▲), dual 1.5-MeV He^+ and 800-keV Cu^+ (○), dual 1.5-MeV He^+ and 1.2-MeV Ag^+ (□), and dual 1.5-MeV He^+ and 300-keV Al^+ (△) irradiations using heavy-ion beam currents which resulted in a total cascade volume production rate of approximately 6.5×10^{12} nm^3/s. For dual beam irradiation experiments, the total dpa represents the sum of dpa from both ion beams. Ion beam currents are given in the legend, while depletion rates, M_{dep}, for the above experiments are listed in Table 2.

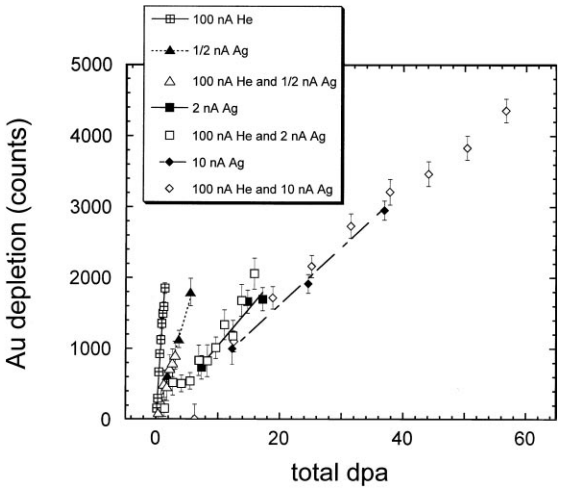

Fig. 8. Au depletion as a function of total dpa for single 1.5-MeV He^+ (⊞), single 1.2-MeV Ag^+ (▲, ■, ◆), and dual 1.5-MeV He^+ and 1.2-MeV Ag^+ (△, □, ◇) irradiations using three Ag^+ beam currents which resulted in total cascade volume production rates of 6.5×10^{12} nm^3/s, 2.58×10^{13} nm^3/s, and 1.29×10^{14} nm^3/s. For dual beam irradiation experiments, the total dpa represents the sum of dpa from both ion beams. Ion beam currents are given in the legend, while depletion rates, M_{dep}, for the above experiments are listed in Table 2.

ΔM_{dep}, for the data in Figs. 6–8 are given in Table 3. Furthermore, since only the segregation rates are being compared, data were translated so that all straight lines passed through the origin.

4. Discussion

4.1. Segregation suppression during dual light- and heavy-ion irradiation

Figs. 6–8 show that simultaneous He^+ and heavy-ion irradiation resulted in Au segregation rates which were significantly lower than that induced by He^+ alone. Iwase et al. [5,12] suggested that putative interactions between short-lived heavy-ion cascade remnants and He^+-generated FMD suppressed RIS by reducing He^+-induced defect fluxes which drive the Au depletion. Long-lived stable sink structures (i.e. dislocations) were not responsible for the RIS suppression observed by Iwase et al., since removal of the Cu^+ beam during dual He^+ and Cu^+ irradiations resulted in the immediate change of the Au depletion rate to that observed during He^+-only irradiation.

As seen in Table 3, the segregation rates, M_{dep}, were the same within experimental error, ΔM_{dep}, for all single heavy-ion irradiations and their respective dual irradiations. Table 3 also shows that M_{dep} values were close to the same (within ΔM_{dep}) for single Al^+, Cu^+, and Ag^+ irradiations producing similar cascade-volume production rates. These observations show that the RIS suppression induced by heavy-ion irradiation correlates well with the calculated cascade-volume production rates. Hence, the RIS suppression rate did not correlate with

Table 3
Au depletion rates in Cu–1at.%Au during various single and dual ion beam irradiations at 400°C. The beam current was 100 nA for 1.5-MeV He^+ in all cases

Ion/current	M_{dep}	ΔM_{dep}
He^+	1360	59
4-nA Al^+	370	26
He^+ and 4-nA Al^+	342	25
20-nA Al^+	133	10
He^+ and 20-nA Al^+	130	7
1-nA Cu^+	339	160
He^+ and 1-nA Cu^+	339	22
5-nA Cu^+	131	29
He^+ and 5-nA Cu^+	143	7
0.5-nA Ag^+	309	30
He^+ and 0.5-nA Ag^+	301	54
2-nA Ag^+	104	23
He^+ and 2-nA Ag^+	114	12
10-nA Ag^+	81	10
He^+ and 10-nA Ag^+	77	4

the total cascade-volume produced per ion, nor with the average primary recoil energy, $T_{1/2}$. Computer modeling by Wiedersich [10,11] assumed that cascade remnant density is independent of cascade size and, hence, only depends on the total cascade-volume production rate during irradiation. The present experimental observations thus lend support to the validity of this assumption.

Iwase et al. [5,12] suggested that $K_{Cu}/K_{He} = 10$ resulted in complete suppression of He^+-RIS because the Au depletion rate was the same for single Cu^+ and dual He^+ and Cu^+ irradiations. Applied to the present experiment, this interpretation would imply that complete suppression of He^+-RIS would have been obtained for 4-nA Al^+, 1-nA Cu^+, and 0.5-nA Ag^+ conditions, as indicated in Fig. 7. However, it is pointed out that the plot of M_{dep} versus total damage dose not provide a consistent indication of complete suppression of He^+-RIS. In fact, if only heavy-ion-induced Au transport occurred during dual 100-nA He^+ and heavy-ion irradiation (i.e., He^+-RIS was completely suppressed), M_{dep} for the dual irradiation would be less than that for single heavy-ion irradiation because the He^+ component of the irradiation would increase the total dpa without increasing the magnitude of Au depletion. The expected value of M_{dep} for complete suppression of He^+-RIS during any dual He^+ and heavy-ion irradiation, M_{dep}^{comp}, should thus be defined as

$$M_{dep}^{comp} = \frac{K_{heavy}}{(K_{heavy} + K_{He})} M_{dep}^{heavy}, \quad (1)$$

where K_{heavy} and K_{He} are the damage rates of the heavy-ion and He^+ beams, respectively, and M_{dep}^{heavy} is the Au depletion rate generated by the single heavy-ion irradiation. An example of M_{dep}^{comp} is demonstrated in Fig. 9 for 4-nA Al^+. Since M_{dep} for dual He^+ and 4-nA Al^+ irradiation is significantly greater than M_{dep}^{comp} for the same conditions, Fig. 9 illustrates that 4-nA Al^+ does not completely suppress He^+-induced Au segregation. The values of M_{dep}^{comp} and associated errors ΔM_{dep}^{comp} are compared with M_{dep} and ΔM_{dep} from the corresponding dual irradiation in Table 4. It is concluded that 4-nA Al^+ and 0.5-nA Ag^+ caused only partial suppression of He^+-RIS since $M_{dep}^{comp} \neq M_{dep}$ within experimental errors. The

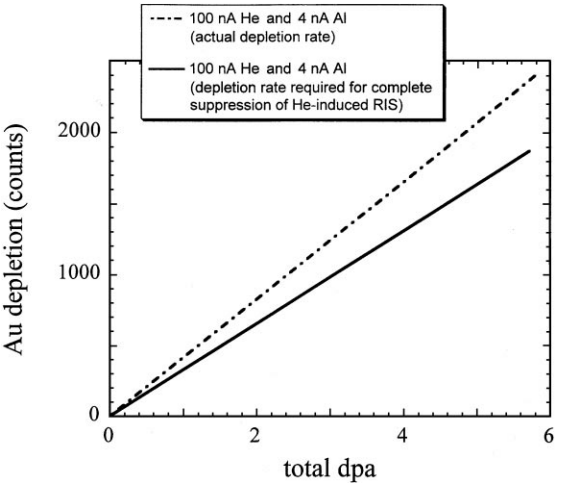

Fig. 9. Comparison of the actual Au depletion rate for a dual 1.5-MeV He^+ and 300-keV Al^+ irradiation (dashed line) and the requisite rate for complete suppression of He^+ RIS (solid line). Since the requisite rate is noticeably lower than the actual rate, complete suppression of He^+ RIS has not been achieved with a 4-nA Al^+ beam. The abscissa represents the sum of dpa from both ion beams. Ion beam currents are given in the legend, while the actual depletion rates, M_{dep}, and the depletion rates required for complete suppression of He^+ RIS, M_{dep}^{comp}, for all dual irradiation experiments are compared in Table 3.

1-nA Cu^+ irradiation resulted in $M_{dep}^{comp} \approx M_{dep}$ within error, but ΔM_{dep}^{comp} was large, relative to all other errors in this investigation. However, the large difference between M_{dep}^{comp} and M_{dep} demonstrated that 1-nA Cu^+ only partially suppressed He^+-produced Au segregation during simultaneous irradiation. On the other hand, 20-nA Al^+, 5-nA Cu^+, and 2-nA Ag^+ completely suppressed He^+-RIS since $M_{dep}^{comp} = M_{dep}$ within ΔM_{dep} and ΔM_{dep}^{comp}.

The effects of three different beam currents of 1.2-MeV Ag^+(0.5, 2, and 10 nA) and, hence, three cascade volume production rates, on He^+ RIS are shown in Fig. 8. It can be seen that increasing Ag^+ beam current resulted in a decrease of M_{dep} during both single Ag^+ and dual He^+ and Ag^+ irradiation. At 400°C, mutual recombination is the primary mechanism for defect annihilation [5,12], and therefore, the reduction in M_{dep}

Table 4
Actual Au depletion rates from dual ion beam irradiations in Cu–1at.%Au at 400°C compared to the requisite rates for complete suppression of He^+ RIS. The beam current was 100 nA for 1.5-MeV He^+ in all cases

Ions/currents	M_{dep}	ΔM_{dep}	M_{dep}^{comp}	ΔM_{dep}^{comp}
He^+ and 4-nA Al^+	342	25	284	20
He^+ and 20-nA Al^+	130	7	125	9
$He^+$and 1-nA Cu^+	339	22	235	110
He^+ and 5-nA Cu^+	143	7	120	27
He^+ and 0.5-nA Ag^+	301	54	211	21
He^+ and 2-nA Ag^+	114	12	93	21

Table 5
Comparison of M_{dep} from 4-nA Al^+, 1-nA Cu^+, and 0.5- and 2-nA 1.2-MeV Ag^+ irradiations with M_{dep} predicted by the (−1/4)-power relationship and M_{dep} from 20-nA Al^+, 5-nA Cu^+, 10-nA Ag^+ irradiations, respectively

Ion/current	Measured M_{dep}	ΔM_{dep}	$(K_{0,1}/K_{0,2})^{-1/4}$	Predicted M_{dep}
4-nA Al^+	427	34	0.67	199
20-nA Al^+	133	10	1	133
1-nA Cu^+	339	160	0.67	196
5-nA Cu^+	131	29	1	131
2-nA Ag^+	104	23	0.67	121
10-nA Ag^+	81	10	1	81

with increasing Ag^+ current for single Ag^+ irradiations should obey the (−1/4)-power relationship [4]:

$$\frac{(dM/d\phi)_1}{(dM/d\phi)_2} = \frac{(M_{dep})_1}{(M_{dep})_2} = \left[\frac{K_1}{K_2}\right]^{-1/4}. \quad (2)$$

Using the experimentally measured M_{dep} from the 10-nA Ag^+ irradiation as $(M_{dep})_1$, the predicted values of M_{dep} for 0.5- and 2-nA Ag^+ irradiations are given in Table 5. Eq. (2) accurately predicted M_{dep} for 2-nA Ag^+, but inaccurately predicted M_{dep} for 0.5-nA Ag^+ by almost a factor of 2. It was also utilized to predict M_{dep} of 1-nA Cu^+ and 4-nA Al^+ from M_{dep} of 5-nA Cu^+ and 20-nA Al^+, respectively (Table 5). As in the 0.5-nA Ag^+case, the predicted M_{dep} were approximately a factor of 2 smaller than the measured values. Thus, M_{dep} follows the (−1/4)-power relationship described by Eq. (2) only when the heavy-ion cascade volume production rate is large enough to suppress all He^+ RIS.

4.2. Phenomenological modeling

In interpreting the experimental results, theoretical modeling of RIS in Cu–1at.%Au alloys was performed, using the kinetic model of Johnson and Lam [1]. Briefly, this model includes the effects of vacancy and interstitial diffusional encounters with solute atoms, as well as the formation, dissociation, and migration of defect-solute complexes. Binding between a vacancy and a solute atom is assumed to be effective only within the first-neighbor distance. The resulting complex 'vs' can migrate without dissociation with energy $H_{vs}^m = H_v^m$, with H_v^m being the vacancy migration energy. On the other hand, if the vacancy and solute atom repel each other (i.e. binding energy $H_{vs}^b < 0$), then $H_{vs}^m = H_v^m - H_{vs}^b$. Interactions between an interstitial (a⟨1 0 0⟩ dumbbell in fcc metals) and a solute atom are assumed to extend to second-neighbor distances, which leads to two types of bound interstitial-solute complexes. Bound complexes 'is(a)' have a greater binding energy than complexes 'is(b)', and migrate as a unit without complete dissociation. The migration energy of is(a) complexes is taken as $H_{is(a)}^m = H_i^m + (3/5)H_{is(a)}^b$ for binding and $H_{is(a)}^m = H_i^m - (1/5)H_{is(a)}^b$ for repulsion, with H_i^m and $H_{is(a)}^b$ being the energies of interstitial migration and is(a)-complex binding, respectively. Bound complexes is(b) are considered to be immobile. The model casts the RIS phenomenon into a set of nonlinear differential equations describing the evolution of the concentrations of the alloying elements and radiation-induced defects in time and space. For a detailed discussion of the migration of complexes, reaction-rate constants, diffusion coefficients, and the resulting rate equations, the reader is referred to the original paper by Johnson and Lam [1].

In the present work, the Johnson–Lam rate equations were solved numerically with the aid of the LSODE package of subroutines [16]. A semi-infinite geometry and appropriate initial and boundary conditions were used for modeling RIS under ion bombardment [17]. Model samples were 13.36-μm thick and divided into 150 sections varying from 0.5 to 300 nm in thickness. The thickness was chosen significantly greater than the range of 1.5-MeV He^+ions (Table 1), necessary to insure proper boundary conditions at the sample's back surface. Damage profiles of all ions were calculated by TRIM-96. For dual irradiation, the effective FMD production rates resulting from the heavy-ion and He^+ beams, K_{heavy} and K_{He}, used in the rate equations for free interstitials and vacancies, were defined as

$$K_0 = \varepsilon_{He}K_{He} + \varepsilon_{heavy}K_{heavy}, \quad (3)$$

where ε_{He} and ε_{heavy} called efficiencies of FMD production by He^+ and heavy ions, respectively, are the fractions of point defects created by these ions that survive recombination and are free to migrate.

The sink concentrations for interstitials and vacancies, assumed to be equal in the calculations, consist of two components: intrinsic sinks, $C_{sin\,k}^o$, and radiation-induced sinks, $C_{sin\,k}^{rad}$. The effective sink strength, $C_{sin\,k}^{total}$, is thus

$$C_{sin\,k}^{total} = C_{sin\,k}^o + C_{sin\,k}^{rad}. \quad (4)$$

$C_{sin\,k}^{rad}$ was scaled to the damage profiles of both He^+ and heavy ions [18,19], and included both extended sinks, such as dislocations, and short-lived cascade remnants. The peak values of $C_{sin\,k}^{rad}$, $C_{sin\,k}^{rad}$ (peak), occurred at the damage peaks. It was not possible to separate the effects of dislocations and remnants on RIS from experimental data, and, therefore, their contributions were not distinguished in the simulations.

Since the modeling yielded the Au concentration as a function of depth, a comparison of model calculations to experimental results was not direct. Therefore, it was necessary to convert the calculated Au depletion values to depletion counts measured experimentally by RBS. The first step was to establish the depth (i.e., energy) resolution of experimental spectra. Using the RSVP code, which generates RBS spectra from a known compositional distribution [20], the depth per channel measured in RBS spectra was determined to be 0.857 nm with the experimental configuration shown in Fig. 1. The next step was to establish a relationship between RBS spectrum depth in the Au plateau region (i.e. channels > 800 of the RBS spectrum shown in Fig. 4(a)) and the number of total Au counts in an unirradiated Cu–1Au sample. Utilizing the depth resolution value with a pre-irradiation (experimental) RBS spectrum, a linear approximation of the relationship between depth from the surface, δ, and total backscattering counts, M_0, from δ to the surface was determined. This relationship is $M_0 = 275\delta$, where δ is in nm. Channels and counts outside the Au plateau region were not considered since all experimentally measured depletion occurred within 100 nm of the surface (well above channel 800 in Fig. 4).

From the calculated Au concentration profile at various irradiation times, the fraction of Au depletion, η, and the depth of the depleted zone, δ, were determined. In turn, the number of equivalent Au depletion counts, M_{dep}, was calculated using the relationship: $M_{\text{dep}} = 275(1-\eta)\delta$. This relationship does not account for Au depletion that occurred during the acquisition of the initial RBS spectrum using 1.5-MeV He^+ at 400°C. However, since the present investigation focused on the change in the rate of segregation during dual ion irradiation and not the exact amount of Au depletion, this approximation did not greatly affect the reported results.

Model calculations were systematically performed for RIS during single He^+, Al^+, Cu^+, and Ag^+ irradiations and fit to the RBS measurements. The fixed parameters used in the modeling were the formation and migration energies of interstitials and vacancies [23–25], and the vibration frequency factors for these point defects and solute-defect complexes, suggested in previous work [17]. Although the values for the formation and migration energies of interstitials and vacancies were experimentally determined for pure Cu [23–25], they were assumed to be applicable to the dilute Cu–1at.%Au alloy. In addition, variations in these parameters with environment were not considered, given the uncertainty in other variables such as radiation-induced sink densities.

First, the best fit for the case of He^+ irradiation produced an optimal set of defect formation, binding and migration energies, listed in Table 6 together with other fixed parameters used, and optimal values of $\varepsilon_{\text{He}} = 0.25$ and $C^{\text{rad}}_{\sin k}(\text{peak}) = 3.1 \times 10^{-4}$ (in atomic fraction). The defect parameters derived are in good agreement with those reported previously by Hashimoto et al. [4]. These authors also found a relative defect-production efficiency of ~0.5 for He^+, relative to H^+. The same relative value was obtained for Ni–Si alloys [21]. On the other hand, based on a comparison of the calculated growth kinetics of the surface γ'-Ni_3Si film with the experimental observations on a Ni–Si alloy undergoing 1-MeV H^+ irradiation at various temperatures, Lam et al. [22] deduced a value of $\varepsilon_{\text{H}} = 0.5$ for H^+, relative to 1-MeV electrons which produce point defects that are all free to migrate. Thus, the value of ε_{He} obtained in the present work is consistent with these combined findings. Then, using the same set of defect parameters, subsequent calculations were carried out for heavy-ion irradiations. The results are plotted with in Figs. 10–12. The derived FMD production efficiencies,

Table 6
Defect parameters utilized in all model calculations for ion-irradiated Cu–1at.%Au

Parameter	Symbol	Value	References/remarks
Formation energy of interstitials	H^{f}_{i}	2.2 eV	[23]
Formation energy of vacancy	H^{f}_{v}	1.3 eV	[24]
Migration energy of interstitials	H^{m}_{i}	0.12 eV	[25]
Migration energy of vacancy	H^{m}_{v}	0.76 eV	[24]
Migration energy of type-a interstitial-solute complexes	$H^{\text{m}}_{\text{is(a)}}$	0.15	$H^{m}_{\text{is(a)}} = H^{m}_{i} - (1/5)H^{b}_{\text{is(a)}}$
Migration energy of solute-vacancy complexes	H^{m}_{vs}	0.76	$H^{m}_{\text{vs}} = H^{m}_{v}$
Binding energy of type-a interstitial-solute complexes	$H^{\text{b}}_{\text{is(a)}}$	−0.14 eV	[4]
Binding energy of solute-vacancy complexes	H^{b}_{vs}	0.03 eV	[4]
Vibration frequency factor for interstitials	ν^0_{i}	5×10^{12} s^{-1}	[17]
Vibration frequency factor for vacancies	ν^0_{v}	5×10^{13} s^{-1}	[17]
Vibration frequency factor for type-a interstitial-solute complexes	ν^0_{is}	5×10^{12} s^{-1}	[17]
Vibration frequency factor for vacancy-solute complexes	ν^0_{vs}	5×10^{13} s^{-1}	[17]
Interstitial-solute-interstitial coupling coefficient	σ_{i}	0	Assumed
Vacancy-solute coupling coefficient	σ_{v}	3	Assumed

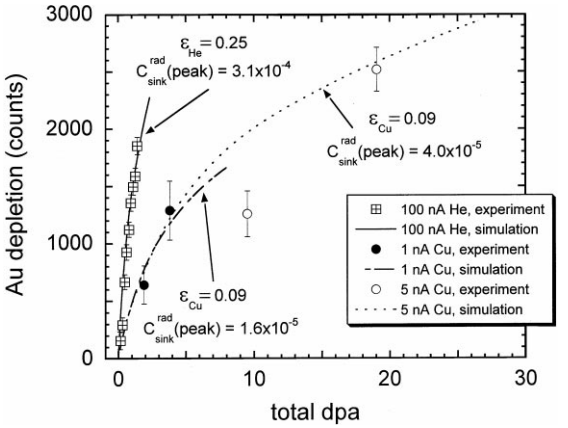

Fig. 10. Comparison of experimental and simulated Au depletion data as a function of total dpa for single 100-nA, 1.5-MeV He^+ (⊞), single 1-nA, 800-keV Cu^+ (●), and single 5-nA, 800-keV Cu^+ (○) irradiations. ε represents the FMD production efficiency of each ion, while C^{rad}_{sink} (peak) represents the peak radiation-induced sink concentration (atom fraction). All other parameters used in the calculations are listed in Table 6.

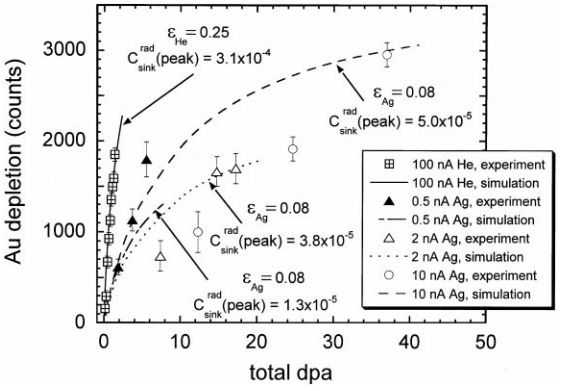

Fig. 11. Comparison of experimental and simulated Au depletion data as a function of total dpa for single 100-nA, 1.5-MeV He^+ (⊞), single 0.5-nA, 1.2-MeV Ag^+ (▲), single 2-nA, 1.2-MeV Ag^+ (△), and single 10-nA, 1.2-MeV Ag^+ irradiations (○). ε represents the FMD production efficiency of each ion, while C^{rad}_{sink} (peak) represents the peak radiation-induced sink concentration (atom fraction). All other parameters used in the calculations are listed in Table 6.

ε_{ion}, and C^{rad}_{sink} (peak) are given in the figures and listed in Table 7.

Using the values of ε_{ion} and C^{rad}_{sink} (peak) derived for single-ion irradiations (Figs. 10–12), dual He^+ and heavy-ion irradiation calculations were performed, and the results are compared with the RBS measurements in Figs. 13–15. In general, the model calculations slightly overestimated the actual amounts of Au segregation, more so in the 1-nA Cu^+ and 0.5-nA Ag^+ cases where

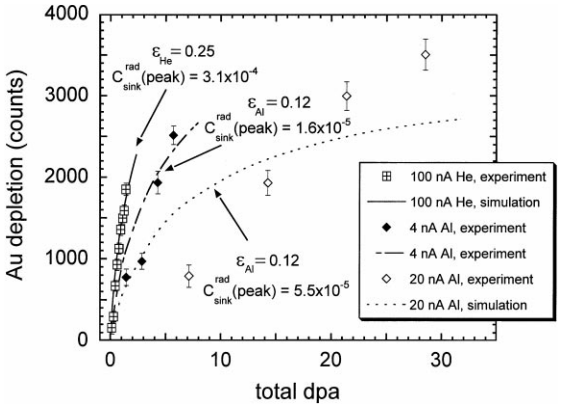

Fig. 12. Comparison of experimental and simulated Au depletion data as a function of total dpa for single 100-nA, 1.5-MeV He^+ (⊞), single 4-nA, 300-keV Al^+ (◆), and single 20-nA, 300-keV Al^+ (◇) irradiations. ε represents the FMD production efficiency of each ion, while C^{rad}_{sink} (peak) represents the peak radiation-induced sink concentration (atom fraction). All other parameters used in the calculations are listed in Table 6.

the cascade-volume production rate was approximately 6.5×10^{12} nm^3/s.

As mentioned previously, C^{rad}_{sink} included both extended sinks (i.e. dislocations) and short-lived sinks (i.e. cascade remnants), and hence it was not possible to determine the exact contribution of each component to FMD annihilation, due to limitations of the experimental data. Therefore, the values of ε_{ion} and C^{rad}_{sink} (peak) could not be estimated independently using the present model. The tested ranges of ε_{ion} and C^{rad}_{sink} (peak), given in Table 7, represent a ±20% deviation from the optimal values when one of these parameters was varied. Further information about radiation-induced sinks needs to be acquired before 'true' efficiencies can be determined.

5. Conclusions

1.5-MeV He^+ and heavy-ion (300-keV Al^+, 800-keV Cu^+, and 1.2-MeV Ag^+) irradiations were performed in Cu–1at.%Au to investigate the interactions between FMDs and cascade remnants which suppress RIS. RBS measurements during single and dual He^+ and heavy-ion irradiations at 400°C demonstrated that the suppression effect of heavy-ion cascade remnants on He^+-RIS corresponded well with the total cascade volume production rate generated by 300-keV Al^+, 800-keV Cu^+, and 1.2-MeV Ag^+ and was independent of the total cascade volume produced per incident heavy ion and of $T_{1/2}$. Au depletion rates as a function of *total* ion damage were the same for single heavy-ion and respective dual He^+ and heavy-ion irradiations, while Au

Table 7
FMD production efficiencies, ε_{ion}, and peak radiation-induced sink concentrations, C^{rad}_{sink} (peak), for all single He^+, Al^+, Cu^+, and Ag^+irradiations. C^{rad}_{sink} (peak) is given in atom fraction, while the ranges represent ε_{ion} and C^{rad}_{sink} (peak) values that produce a ± 20% deviation in Au depletion level from the 'optimum' parameters

Ion/current	Optimal ε_{ion}	Optimal C^{rad}_{sink} (peak) (10^{-5})	Tested range for ε_{ion}	Tested range for C^{rad}_{sink} (peak) (10^{-5})
100-nA He^+	0.25	31	0.21–0.30	26–37
4-nA Al^+	0.12	1.6	0.10–0.16	1.2–2.0
20-nA Ag^+	0.12	5.5	0.08–0.20	4.0–7.5
1 nA Cu^+	0.09	1.6	0.08–0.10	1.4–1.8
5-nA Cu^+	0.09	4.0	0.07–0.13	3.0–5.0
0.5-nA Ag^+	0.08	1.3	0.07–0.09	1.25–1.5
2 nA Ag^+	0.08	3.8	0.07–0.10	3.2–4.5
10-nA Ag^+	0.08	5.0	0.05–0.16	3.3–7.3

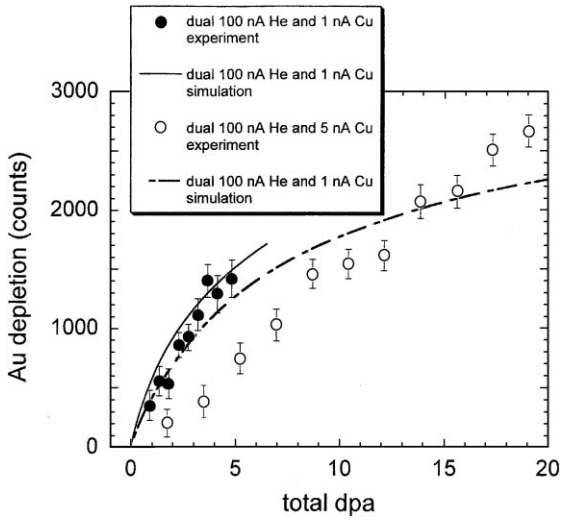

Fig. 13. Comparison of experimental and simulated Au depletion data as a function of total dpa for dual 100-nA, 1.5-MeV He^+ and 1-nA, 800-keV Cu^+ (●) and dual 100-nA, 1.5-MeV He^+ and 5-nA, 800-keV Cu^+ (○) irradiations. ε and C^{rad}_{sink} (peak) values are given in Table 5, and all other parameters used in the calculations are listed in Table 6.

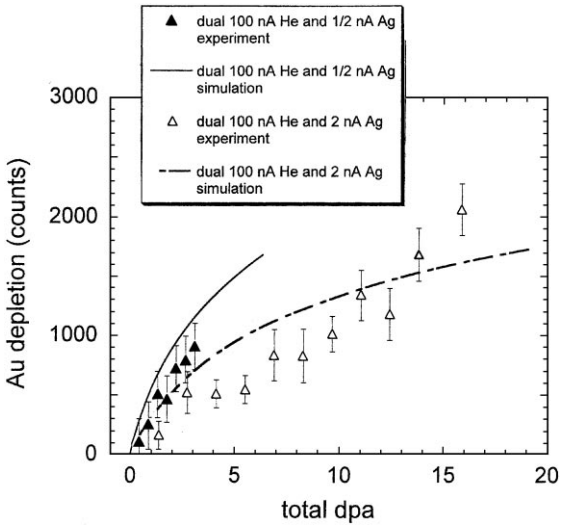

Fig. 14. Comparison of experimental and simulated Au depletion data as a function of total dpa for dual 100-nA, 1.5-MeV He^+ and 0.5-nA, 1.2-MeV Ag^+ (▲) and dual 100-nA, 1.5-MeV He^+ and 2-nA, 1.2-MeV Ag^+ (△) irradiations. ε and C^{rad}_{sink} (peak) values are given in Table 5, and all other parameters used in the calculations are listed in Table 6.

depletion rates for all single heavy-ion irradiations were the same and nearly the same for cascade-volume production rates of 3.0×10^{13} nm^3/s and 6.5×10^{12} nm^3/s, respectively. RBS results also demonstrated that only partial suppression of 1.5-MeV He^+-induced segregation was achieved by heavy-ion cascade remnants during dual He^+ and heavy-ion irradiations at 6.5×10^{12} nm^3/s, while complete suppression was attained at 3.0×10^{13} nm^3/s.

During all single heavy-ion irradiations, recombination was the dominant mechanism of FMD annihilation, and Au depletion rates (as a function of total ion damage) should obey a $(K_1/K_2)^{-1/4}$ damage-rate dependence at cascade-volume production rates greater than 3.0×10^{13} nm^3/s (i.e., large enough to completely suppress He^+-generated segregation). Below this cascade-volume production rate, the $(K_1/K_2)^{-1/4}$ prediction underestimated the Au depletion rate by approximately a factor of 2.

Simulations of RIS during both single and dual irradiations were also performed using the Johnson–Lam model. The model was slightly modified to include the effects of radiation-produced extended sinks and cascade remnants, which were effectively accounted for in the same sink-annihilation term in the rate equations. In general, good fits of model calculations to the RBS measurements were obtained; in a few cases, however, the model overestimated the amount of Au depletion.

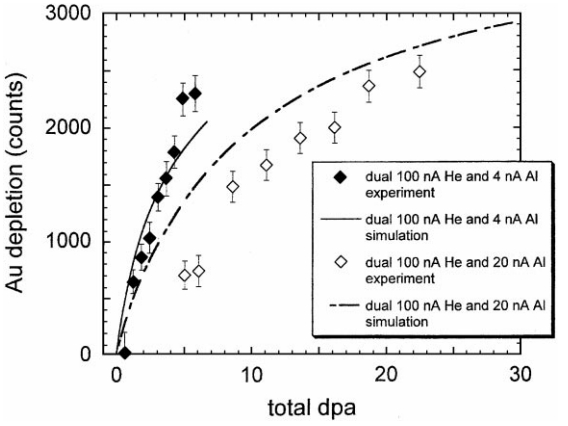

Fig. 15. Comparison of experimental and simulated Au depletion data as a function of total dpa for dual 100-nA, 1.5-MeV He^+ and 4-nA, 300-keV Al^+ (◆) and dual 100-nA, 1.5-MeV He^+ and 20-nA, 300-keV Al^+ (◇) irradiations. ε and C^{rad}_{sink} (peak) values are given in Table 5, and all other parameters used in the calculations are listed in Table 6.

Information regarding the solute-defect binding and migration energies, free-defect production efficiencies, and radiation-induced defect sink concentrations were derived from the best fits. The optimal values for these parameters are summarized in Tables 6 and 7. For example, using the values previously reported for the energies of formation and migration for vacancies and interstitials in Cu, the binding and migration energies of Au–interstitial and Au–vacancy complexes in the alloy were found to be $H^b_{is(a)} = -0.14, H^m_{is(a)} = 0.15$, and $H^b_{vs} = 0.03$ and $H^m_{vs} = 0.76$ eV, respectively. The derived efficiencies of freely migrating defect production by energetic He^+, Al^+, Cu^+, and Ag^+ ions were, respectively, $\varepsilon_{He} = 0.25$, $\varepsilon_{Al} = 012$, $\varepsilon_{Cu} = 0.09$, and $\varepsilon_{Ag} = 0.08$. Further experimental information about radiation-induced sinks will be necessary to accurately model the effects of cascade remnants on RIS kinetics.

Acknowledgements

The authors wish to thank D. E. Alexander, J. Heuer, A. Iwase, and P. R. Okamoto for helpful discussions. They are also grateful to B. Kestel for valuable technical assistance in sample preparation. This work was supported by the US Department of Energy, Office of Science, under Contract No. W-31-109-Eng-38.

References

[1] R.A. Johnson, N.Q. Lam, Phys. Rev. B 13 (1976) 4364.
[2] P.R. Okamoto, L.E. Rehn, J. Nucl. Mater. 83 (1979) 2.
[3] H. Wiedersich, N.Q. Lam, in: F.V. Nolfi Jr. (Ed.), Phase Transformations During Irradiation, Applied Science, London, 1983, p. 1.
[4] T. Hashimoto, L.E. Rehn, P.R. Okamoto, Phys. Rev. B 38 (1988) 12868.
[5] A. Iwase, L.E. Rehn, P.M. Baldo, L. Funk, Appl. Phys. Lett. 67 (1994) 229.
[6] R.A. Erck, L.E. Rehn, J. Nucl. Mater. 168 (1989) 208.
[7] R.S. Averback, J. Nucl. Mater. 216 (1994) 49.
[8] T. Muroga, S. Ishino, J. Nucl. Mater. 117 (1983) 36.
[9] D.J. Bacon, T. Diaz de la Rubia, J. Nucl. Mater. 216 (1994) 275.
[10] H. Wiedersich, Mater. Sci. Forum 97–99 (1992) 59.
[11] H. Wiedersich, J. Nucl. Mater. 205 (1983) 40.
[12] A. Iwase, L.E. Rehn, P.M. Baldo, L. Funk, J. Nucl. Mater. 238 (1996) 224.
[13] A. Iwase, L.E. Rehn, P.M. Baldo, L. Funk, J. Nucl. Mater. 244 (1997) 147.
[14] P. Lucasson, in: M.T. Robinson, F.W. Young, Jr. (Eds.), Fundamental Aspects of Radiation-Damage in Metals, CONF-751006P1, National Technical Information Service, Springfield, VA, 1975, p. 42.
[15] H.F. Deng, D.J. Bacon, Phys Rev. B 53 (1996) 11,376.
[16] A.C. Hindmarsh, in: R.S. Stepleman et al. (Eds.), Scientific Computing, North-Holland, Amsterdam, 1983, p. 55.
[17] N.Q. Lam, P.R. Okamoto, R.A. Johnson, J. Nucl. Mater. 78 (1978) 408.
[18] N.Q. Lam, G.K. Leaf, J. Mater. Res. 1 (1986) 251.
[19] P. Fielitz, M.-P. Macht, V. Naundorf, H. Wollenberger, J. Nucl. Mater. 251 (1997) 123.
[20] R.S. Averback, L.J. Thompson Jr., J. Moyle, M. Scalit, J. Appl. Phys. 53 (1982) 1342.
[21] L.E. Rehn, P.R. Okamoto, Mater. Sci. Forum 15–18 (1987) 985.
[22] N.Q. Lam, T. Nguyen, G.K. Leaf, S. Yip, Nucl. Instrum. and Meth. B 31 (1988) 415.
[23] W. Schilling, J. Nucl. Mater. 69&70 (1978) 465.
[24] R.W. Siegel, in: J. Takamura, M. Doyama, M. Kiritani, (Eds.), Point Defects and Defect Interactions in Metals, University of Tokyo Press, 1982, p. 533.
[25] F.W. Young, J. Nucl. Mater. 69&70 (1978) 310.